iScience

CellPress
OPEN ACCESS

Article

Revealing the detrimental CO_2 reduction effect of $La_{0.6}Sr_{0.4}FeO_{3-\delta}$-derived heterostructure in solid oxide electrolysis cells

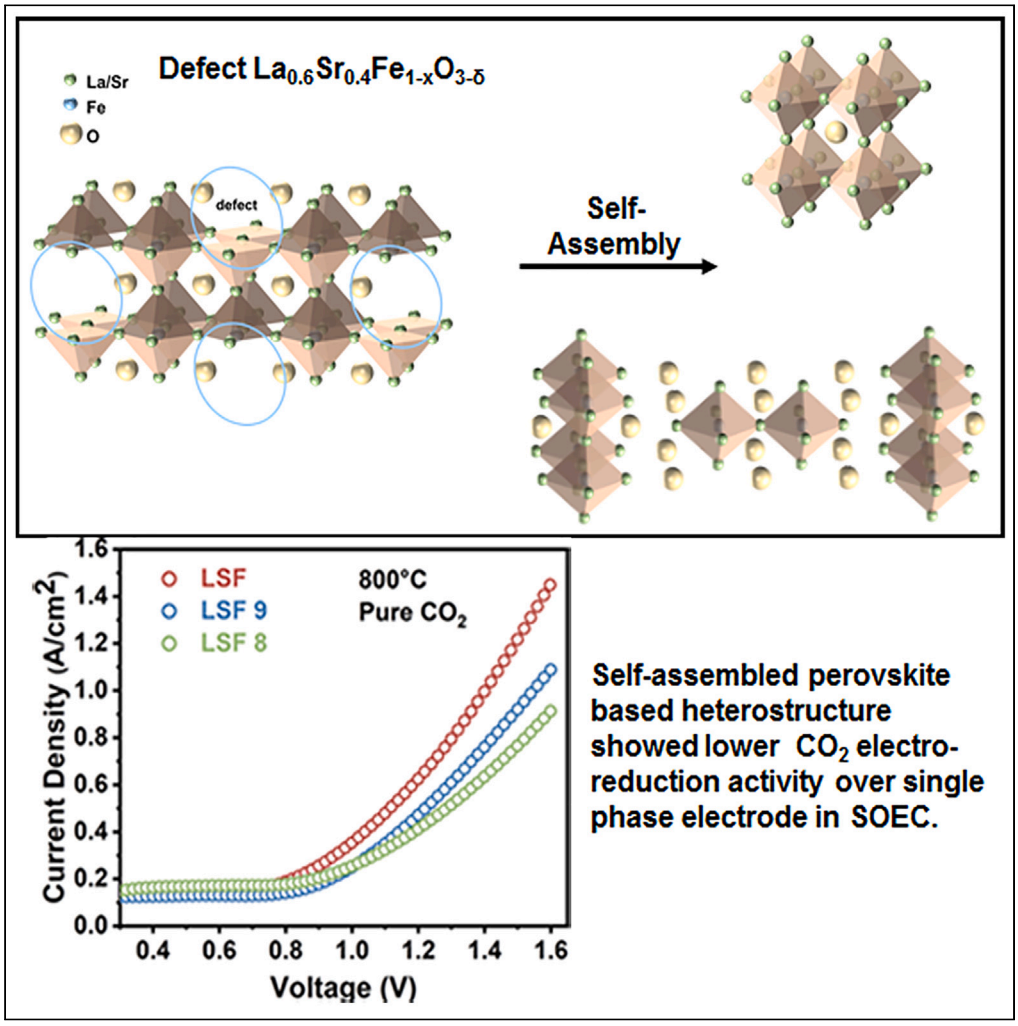

Rui Yang, Wanbin Lin, Yunjuan He, Manish Singh, Liangdong Fan

heyunjuan1988@163.com (Y.H.)
fanld@szu.edu.cn (L.F.)

Highlights

Synthesis of two-phase perovskite composite by the self-assembly method

The negative effect of heterogeneous structures on CO_2 electrolysis

Reduced oxygen vacancy and conductivity, increased Fe valence and Sr aggregation

Kinetics CO_2 reduction on heterogeneous perovskite oxide in SOECs

Yang et al., iScience 27, 109648
May 17, 2024
https://doi.org/10.1016/j.isci.2024.109648

iScience

CellPress
OPEN ACCESS

Article

Revealing the detrimental CO_2 reduction effect of $La_{0.6}Sr_{0.4}FeO_{3-\delta}$-derived heterostructure in solid oxide electrolysis cells

Rui Yang,[1] Wanbin Lin,[1] Yunjuan He,[2,*] Manish Singh,[3] and Liangdong Fan[1,4,*]

SUMMARY

Solid oxide electrolysis cells hold unique Faraday efficiency and favored thermodynamic/kinetics for CO_2 reduction to CO. Perovskite oxide–based composite materials are promising alternatives to Ni-based cermet electrodes in SOECs. However, contrary results of the electrocatalytic activity over single-phase perovskite oxide exist and the rationale of the negative effect is not well revealed. In this work, two-phase perovskite materials with various complementary properties and unique interfaces are self-assembled, which was realized by "subtractive" defect-driven phase separation. The obtained heterostructure electrodes showed reduced performance over that of single-phase materials although the cyclic stability was improved. The main reasons for the performance degradation are the decrease of electrical conductivity, oxygen vacancy concentration while increasing the average valence state of B-site Fe cations, and electrode surface Sr aggregation. This work highlights the self-assembly method and insight into the rational design and synthesis of active electrodes/catalysts for CO_2 conversion in solid oxide cells.

INTRODUCTION

Solid oxide electrolysis cell (SOEC), a device that converts electrical energy and thermal energy into chemical energy, has the advantages of high efficiency and environmental protection.[1,2] In particular, the use of SOEC for CO_2 electrolysis to produce sustainable fuels/chemicals can not only stores renewable energy but also is a perfect solution to complete the task of carbon neutrality and to alleviate the greenhouse effect.[3,4] However, the electrolytic efficiency of SOEC is limited by the catalytic activity of the cathode due to the linear nature of CO_2 molecules and high C=O binding energy, so over the years, researchers have conducted many studies on the development of highly active electrode materials for efficient CO_2 activation and reduction.[5–7] In recent years, Ni-based cermet cathodes like Ni-YSZ (nickel-yttrium stabilized zirconia) were first reported because of their high electrical conductivity and superb catalytic activity for CO_2 reduction reaction (CO_2-RR).[8,9] However, it still suffers from a series of problems, such as carbon deposition and grain aggregation, which makes the long-term application of Ni-based cermet materials in SOEC problematic.[10–12]

To date, perovskite materials with mixed ionic-electronic conducting properties, excellent resistance to carbon deposition, and good cycle stability have received constant attention as alternatives to Ni-cermet electrodes for CO_2 reduction in SOECs.[13,14] Representative materials such as $La_{0.2}Sr_{0.8}TiO_{3+\delta}$ (LST),[15] $Sr_2Fe_{1.5}Mo_{0.5}O_{6-\delta}$ (SFM),[16–18] $La_{0.75}Sr_{0.25}Cr_{0.5}Mn_{0.5}O_{3-\delta}$ (LSCM),[19,20] and (La, Sr)$FeO_{3-\delta}$ (LSF)[21,22] have been well explored. Besides, many methods have been proposed to increase the catalytic activity, such as A-site,[20,23] B-site doping,[24,25] and anion element doping,[21,26] as well as cation deficiency projects.[27] However, there is always a limit to the modification of single-phase materials and the performance gap remains compared with the Ni-based electrode. Alternative electrodes with improved CO_2 chemical adsorption, activation, and facilitated ionic/charge transfer capability are still needed.

Recently, heterostructure catalysts generally composing of active material and various functional additives demonstrated improved electrocatalytic performance toward CO_2-RR.[27–29] Researchers tried to develop a composite electrode material with a heterogeneous interface based on the above materials.[30,31] For example, the heterogeneous interface between perovskite and metal constructed by *in situ* exsolution possesses both good ion conductivity of perovskite and good electrical conductivity of metals.[32,33] Previous works in our group also demonstrated that the constructed heterogeneous interface composed of carbonate and perovskite though *in situ* A-site deficiency and surface carbonate deposition induced by the addition of low valence alkali metal ions with high basicity and low electronegativity enhanced CO_2 adsorption, dissociation process, and CO desorption primitive steps.[20,23] Furthermore, many works also adopted the method of self-assembly to construct heterogeneous interfaces to combine the advantages of each phase. Demont et al.[34] doped large radius W or Mo into $Ba_{0.5}Sr_{0.5}Co_{0.7}Fe_{0.3}$(BSCF) to form B-site cation ordered double perovskite and disordered single perovskite oxide phases. Song et al.[35]

[1]Department of New Energy Science & Technology, College of Chemistry and Environmental Engineering, Shenzhen University, Shenzhen 518060, Guangdong, China
[2]Institute of Energy Power Innovation, North China Electric Power University, Beijing, China
[3]Department of Metallurgical and Materials Engineering, Indian Institute of Technology Patna, Bihta, Bihar 801106, India
[4]Lead contact
*Correspondence: heyunjuan1988@163.com (Y.H.), fanld@szu.edu.cn (L.F.)
https://doi.org/10.1016/j.isci.2024.109648

synthesized a nanocomposite $Sr_{0.9}Ce_{0.1}Fe_{0.8}Ni_{0.2}O_{3-\delta}$, which was self-assembled to a single perovskite phase and a Ruddlesden–Popper phase, accompanied by surface-decorated NiO and CeO_2 minor phases, both showed improved catalytic activity toward the targeted reactions[36,37] However, the process of modification of the composite structure may bring negative effects. Zhu et al.[10] studied that the Fe and Ni cations in the $Sr_2Fe_{1.5-x}Ni_xMo_{0.5}O_{6-\delta}$ (x = 0, 0.05, 0.1, 0.2) that are exsolved and aggregated at the surface of perovskite oxide and reduced to metal nanoparticles did not improve the CO_2 reduction performance as expected because of the severe $SrCO_3$ formation on the surface of the perovskite. Luo et al.[38] also mentioned that the formation of B-site vacancies in perovskite scaffolds because of metal nanoparticle exsolution was the major contributor to the degradation of perovskite activity for CO_2 splitting, while the B-site supplement endows appealing electrochemical performance of both stability and activity for CO_2 reduction.

Thus, self-assembly has been verified as an effective method for synthesizing perovskite oxide-based composite nanocrystals.[38–40] However, the performance of resulting heterogeneous catalysts is often difficult to be predicted. The originality of the negative results should be carefully discussed and more general cases should be reported. In this work, we synthesized a heterostructural phase material containing single-phase (SP) perovskite and Ruddlesden–Popper (RP) phase perovskite from the precursor of $La_{0.6}Sr_{0.4}FeO_{3-\delta}$ perovskite oxide by intentionally adjusting B-site defects/stoichiometry. Different from the previous strategy of "doing addition" (Adding different elements), we use the strategy of "doing subtraction" *in situ* to construct such a heterostructure. In this way, we exclude the influence of conventional *in situ* exsolved metal particles and focus on the role of SP-RP oxide/oxide heterostructures. It is found that the resultant SP-RP heterostructures did not bring a positive effect on CO_2 reduction performance. On the contrary, a detrimental effect was revealed with the increased B-site non-stoichiometry even though the operational stability is improved. The rationale for the reduced CO_2 splitting performance on the oxide-oxide heterostructural interface is carefully analyzed and discussed based on extensive material physical and chemical properties investigation.

RESULTS AND DISCUSSION

Powders' XRD and their refinement results are shown in Figure 1. The as-synthesized $La_{0.6}Sr_{0.4}FeO_{3-\delta}$ (LSF) powders exhibit a pure single perovskite phase with an R-3c:H space group (Figure 1C), while the samples of $La_{0.6}Sr_{0.4}Fe_{0.9}O_{3-\delta}$ (LSF9) and $La_{0.6}Sr_{0.4}Fe_{0.8}O_{3-\delta}$ (LSF8) exhibit one additional phase besides LSF, a Ruddlesden-Popper perovskite phase (RP, PDF card No. 71–1774) appeared with the increased B-site defects (Figures 1D and 1E). The mass ratios of the RP phase in LSF9 and LSF8 are 10.56 wt. % and 27.87 wt. %, respectively (Figures 1C–1E and Table S1). The RP phase content of the samples, which were synthesized by self-assembly, increases gradually with the decrease of the B-site element non-stoichiometry. Due to excessive B-site defects, the cubic perovskite molecule is changed into a layered RP phase during the phase formation process (Figure 1B). According to the detected phase in XRD results, the self-assembly processes can be expressed by the following Equation 1:

$$La_{0.6}Sr_{0.4}Fe_{1-x}O_3 \rightarrow yLa_{0.6}Sr_{0.4}FeO_{3-\delta} + zLa_{1.2}Sr_{0.8}FeO_{4+\delta} \quad \text{(Equation 1)}$$

Where 1-x = y + z based on the Fe element stoichiometry, together with the phase with "O_4" represents the RP perovskite phase characteristics in a layered feature along the c-axis (Figure 1B). The theoretical stoichiometric ratio of La and Sr in Equation 1 is 6:4, but in the actual self-assembly process, their stoichiometric ratio may change to diversify the products. The above results indicated that the composite structural materials were successfully synthesized by intentional B-site stoichiometry adjusting, "doing subtraction" instead of classic "doing addition". Although the composition and proportions of each phase vary, their microstructures are very similar (Figure S1), which will help exclude the influence of microstructure on CO_2 electrolysis.

To further verify the complete heterostructural characteristics of LSF8, the texture structure of LSF8 was visually characterized by TEM (Figure 1F). Two different phases can be seen in the image; the lattice spacing of 0.351 nm represents the (111) planes of single-phase LSF (SP-LSF) and 0.251 nm represents the (112) planes of Ruddlesden-Popper phase (RP-LSF) (more information of lattice spacing parameters of SP and RP phase can be referred to Figure S2), which is consistent with the XRD refinement results (Figures 1C–1E). Between the SP phase and RP phase in the TEM image, an apparent consecutive heterogeneous interface can be found. Those further illustrate the successful synthesis of composite materials and the presence of heterogeneous interfaces with connected channels between different phases.

We continue to evaluate the catalytic activity of the various electrodes for CO_2 reduction in SOECs based on LSGM electrolyte-supported configuration with LSCF-SDC anode and LSFx cathodes under a 100% CO_2 atmosphere. The electrochemical performances are shown in Figures 2A–2E. As can be seen from Figure 2A, with the reduction of the Fe stoichiometric ratio at the B-site, the CO_2 electrolysis performance of single cells deteriorates. The exact CO_2 electrolysis current densities of single cells with the single phase LSF, LSF9, and LSF8 electrodes were 1.22, 0.94, and 0.77 A cm^{-2} at 1.5 V and 800°C, respectively. The corresponding current densities at other temperatures (750 and 850°C) shared a similar tendency (Figure S3). Moreover, the EISs of single cells with different cathode materials were also investigated. Generally, the ohmic resistance (Ro) is the spectra intercept with the real axis at high frequency, while the total electrode polarization resistance (Rp) is calculated from the distance between the two intercepts of the depressed arcs with the real axis.[16] As shown in Figure 2B and Figures S4 and S5, the Ro of LSF, LSF9, and LSF8 are 0.4, 0.52, and 0.61 Ω cm^2 respectively, and the Rp is 0.13, 0.16, and 0.21 Ω cm^2, respectively. Both the ohmic resistance and polarization resistance of single cells increase as the proportion of the RP phase increases. Generally, ohmic resistance is mainly composed of the resistance values of the electrolyte and is also related to the electronic conductivity of the electrode.[4] Since electrolytes' thickness and cells' manufactory processes are the same, the increase in ohmic resistance should be due to the insufficient electrical conductivity of the applied cathodes. For verifying such a hypothesis, the electrical conductivities of LSF, LSF8, and RP-LSF samples in air (oxidizing atmosphere) and 95: 5 CO_2-CO (reducing atmosphere) were measured. Prior to this, the phase structure of different powders at calcination

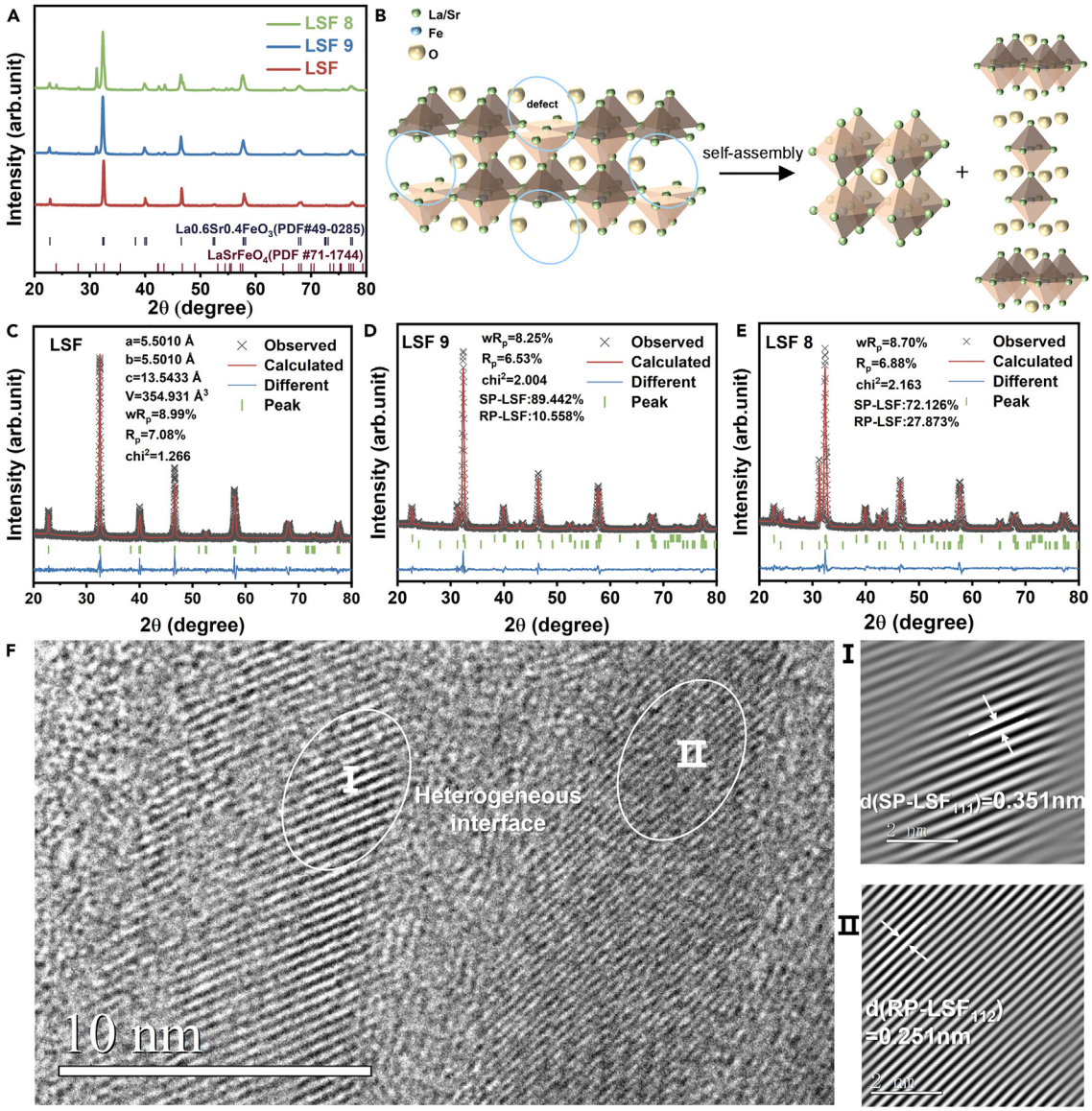

Figure 1. Phase structures and lattice texture of prepared powders samples

(A) XRD, (B) schemetic illustration model of the phase structural transformation through self-assembly process.

(C–E) the corresponding XRD refinement results, and (F) high-resolution TEM image and the selected area lattice texture.

temperature (1300°C) are also verified in Figure S6 to ensure the reliability of the conductivity test. Compare with fresh samples the powders calcined at 1300°C just exhibited slightly different crystallinity and had no effect on the conductivity test.[41] The electrical conductivity of LSF and LSF8 samples in an oxidizing atmosphere and reducing atmosphere both reveal a transition from semiconductor-like to metal-like behavior[42–44] (Figures 2C and S7), i.e., the electrical conductivity first increases with increasing temperature until it reaches a maximum, then decreases with temperature subsequently. In addition, the electrical conductivity of RP-LSF is almost negligible compared to LSF. Those results confirm that the decrease in LSF8 conductivity is precisely due to the introduction of RP-LSF. As expected, the electrical conductivity of LSF8 is lower than LSF in both atmospheres, leading to the increased Ro in the CO_2 electrolysis condition. Such a phenomenon is consistent with the conclusions from other articles.[45] In addition, the electrical conductivity of RP-SLF, in both oxidizing and reducing atmospheres increases with the increase in temperature (Figure S7), showing a simple semiconductor-like behavior. Perhaps it is the absence of metal-like properties that leads to the extremely low conductivity of RP-LSF.

The electrochemical stability of the single cells was also verified. The short-term CO_2 electrolysis stability at 1.5, 1.4, 1.3, and 1.2 V on single cells with LSF, LSF8, and LSF9 fuel electrodes and each for 20 min is shown in Figure 2D. We can find that LSF showed higher resulting initial current density at voltages above 1.3 V over other samples, and its performance severely decreased with the applied time. When being

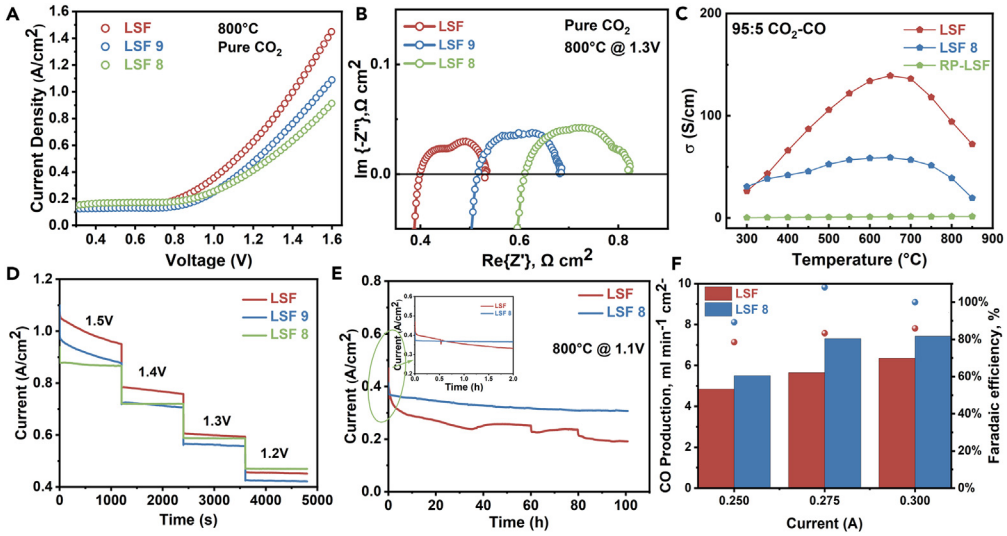

Figure 2. Electrochemical performance of SOECs based on different cathode materials in pure CO_2 atmosphere and at 800°C

(A) I-V curves.

(B) EIS curves at 1.3V, (C) electrical conductivity in 95: 5 CO_2-CO atmosphere, (D) short-term stability, (E) long-term stability at 1.1V, 800°C, and (F) CO production and faradaic efficiency of LSF and LSF8 with different current densities at 800°C.

operated at 1.2 V, the electrolytic current density of the LSF8 electrode under the same voltage exceeded the LSF. Among these, the single cells with an LSF fuel electrode exhibited exaggerated performance degradation, while the single cell with an LSF8 fuel electrode showed wonderful stability under the same circumstances. The I-V curves (Figure S8) after short-term CO_2 electrolysis stability can further verify this conclusion. To further compare the difference in stability, a comparison of long-term CO_2 electrolysis stability tests with LSF and LSF8 fuel electrodes was also performed and the results are shown in Figure 2E. The current density of the single cell with the LSF8 fuel electrode dropped from 0.37 A cm^{-2} to 0.31 A cm^{-2} at 1.1 V for 100 h, while that of the LSF fuel electrode dropped from 0.42 A cm^{-2} to 0.19 A cm^{-2} at the same condition. Furthermore, the performance of a single cell with an LSF electrode decayed below the LSF8 electrode within 1 h, which is consistent with short-term stability results. Apart from the operation stability, the production rate and faradaic efficiency are also considered for the practical application of CO_2 electrolysis. As shown in Figure 2F, the CO production rate of LSF8 (5.50, 7.31, and 7.42 mL min^{-1} cm^{-2}) has surpassed LSF (4.84, 5.65 and 6.35 mL min^{-1} cm^{-2}) at 0.25, 0.275 and 0.3 A. The faradaic efficiency of LSF8 is almost 100% in most circumstances[32] while LSF is only about 80%. The reduced Faraday efficiency of CO_2 reduction on the LSF electrode surface may be ascribed to the additional reaction pathway, such as a CO_2 completely decomposed reaction: $CO_2 \rightarrow C + O_2$. Anyway, despite the reduced catalytic activity, better stability, CO production rate, and faradaic efficiency suggested the superiority of composite structure materials in potential industrial applications.

In Figure 2B, we can see that the electrode polarization resistance (Rp) gradually increased with the applied B-site defects/non-stoichiometry. Although the different sources are ascribed to the cathode, polarization resistance from the anode complexed its deconvolution. To further evaluate the influence of phase transformation on the catalytic activity in terms of the CO_2 reduction reaction, the electrochemical impedance spectra (EIS) data using LSGM electrolyte-supported symmetrical cells were acquired. Symmetrical cells with LSF/LSF9/LSF8 electrodes were operated at open circuit voltages (OCV) conditions at different temperatures and atmospheres. As shown in Figure 3A, the R_p values of LSF, LSF9, and LSF8 electrodes are 0.33, 0.39, and 0.52 Ω cm^{-2} at 800°C in 1: 1 CO_2: CO atmosphere respectively. Obviously, with the decrease of the stoichiometric ratio of the B-site element, the R_p values of heterostructural electrodes increased, which is consistent with the results obtained in single cells. DRT is a useful tool to analyze the complicated electrochemical process which contains different sub-steps.[3] According to literature,[17,21,24,32,42,46] the peaks of CO_2 reduction in SOECs can be divided into three peaks: high frequency (HF, 10^4–10^5 Hz) peaks which is linked to O^{2-} transportation at the interface between the electrode and electrolyte, intermediate frequency (IF, 10^3–10^4 Hz) peaks which are associated with the charge transfer or CO_2 activation process in electrode and low frequency (LF, 10^0–10^3 Hz) peak which indicates gas-related process including adsorption, activation, and dissociation process. As shown in the DRT of LSF at 800°C in 1: 1 CO_2: CO, the spectra show the standard three peaks (Figure 3D). When the stoichiometric ratio of the B-site Fe element in LSF is reduced to 0.9 and 0.8, all frequencies exhibit resistance to a higher value, and a brand-new low-frequency peak P4 gradually emerges (Figures 3D–3F). The reason for the increase of HF and LF in LSF9 and LSF8 is the decrease in their electrical conductivity (Figure 2C), increasing the resistance values of the HF and IF processes representing the O^{2-} and e^- transportation in the electrode and the interface between the electrode and electrolyte. The variation of LF can be attributed to the changes in CO_2 chemical adsorption and activation ability caused by the intervention of the RP phase and heterostructure. We can also find that the low frequency part still occupies the dominant position and is the rate-determining step of the whole CO_2-RR process.

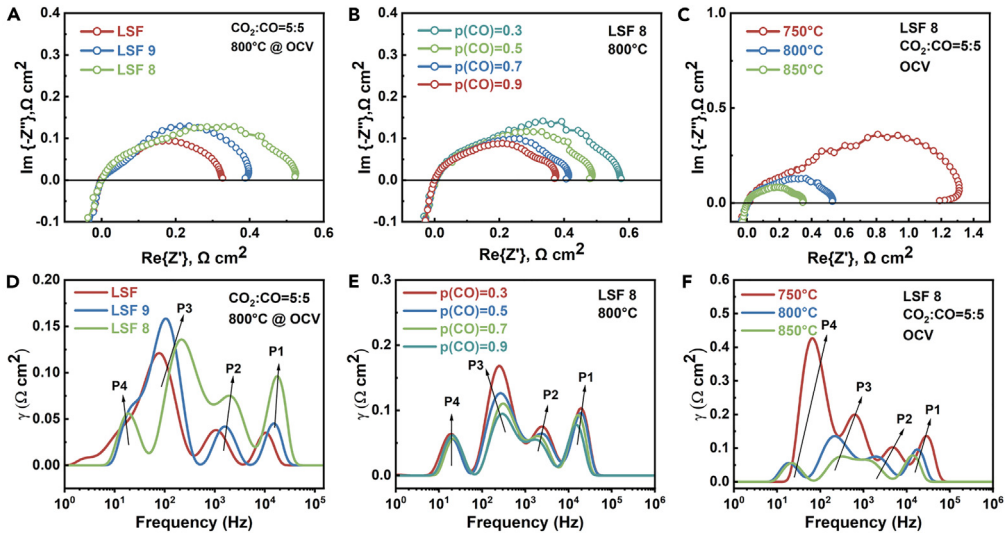

Figure 3. Electrochemical performances of electrolyte-supported symmetrical cells with LSF, LSF9, and LSF8 electrodes at OCV

(A) EIS at 800°C.

(B) EIS of LSF8 under different applied gas atmospheres.

(C) EIS of LSF8 at different temperatures and (D–F) their corresponding DRT curves.

For further analysis, EIS and DRT data of LSF, LSF8, and LSF9 symmetrical cells under different applied gas atmospheres and voltages were also received (Figure S9). The EIS values of the three samples decrease with the increase of the temperature and CO_2 partial pressure. For LSF, all processes are influenced by temperature, while HF and IF processes, which signify the O^{2-} and e^- transportation, are almost independent of the CO_2 partial pressure (Figure S9). For LSF9 and LSF8, all of their processes are also influenced by temperature, but unlike LSF, the HF and IF are also affected by the CO_2 partial pressure (Figures 3 and S9). This result illustrates that the RP phase has the same reaction process as the SP phase, but due to the difference in catalytic activity, it changes the law of change of P1 and P2 peaks under different CO_2 partial pressures. However, the characteristic peak P4 of LSF8 composite material is not affected by the CO_2 partial pressure which is affected by the activation process in CO_2-RR and CO oxidation processes, so P4 may be summarized as a pure adsorption peak occurring on the RP phase and the interface between two phases.[47] It's worth noting that, compared with the LSF8 sample, the variation of DRT of the LSF9 sample is more similar to LSF, which indicates that LSF8 has the complete characteristics of heterogeneous structure and composite materials. The content of the RP-LSF in LSF8 favors forming a continuous channel and may play an important role over that in LSF9. Furthermore, the P4 peak is greatly influenced by temperature (Figure 3F), which further proves that is related to the adsorption process.

To further explore the reasons for the worsening electrochemical performance of the heterostructure material electrodes in single cells and symmetrical cells, the physical and chemical properties of the surface and bulk phase of LSF, LSF9, and LSF8 are explored by XPS, TGA, and CO_2-TPD techniques. As shown in Figure 4A, the Fe $2p_{3/2}$ spectrum can be deconvoluted into 709.6, 710.8, and 712.9 eV three peaks, each represents the Fe^{2+}, $Fe^{3+,}$ and Fe^{4+}. The calculated average valence states of Fe in LSF, LSF9, and LSF8 are 2.562, 2.630, and 2.684, respectively (Table S2), which is reasonable since it helps to make the charge balance with the reduced Fe content in bulk materials. The electronic conduction in perovskite structure is realized via B-site (transition metal) lattice ions through overlapping B-O-B bond via Zerner double exchange process as shown in the Equation 2 [13]:

$$B^{n+} - O^{2-} - B^{(n+1)+} \rightarrow B^{(n+1)+} - O^{2-} - B^{(n+1)+} \rightarrow B^{(n+1)+} - O^{2-} - B^{n+} \quad \text{(Equation 2)}$$

Therefore, the charge density around the B-site atoms and the overlap of B-O will determine the electrical conductivity of perovskite oxide. So, the average valence of Fe can provide a strong basis for the variation of electrical conductivity of different samples. To maintain charge equilibrium, as the stoichiometric ratio of the Fe element in the B-site decreases, the average valence of Fe continues to rise which means a decrease in the density of the surrounding electrons. This could also explain the reason for the decrease in conductivity in Figure 2C and reduced CO_2 reduction activity.[17,41,42] Figure 4B exhibits the XPS spectra of O 1s in as-synthesized LSF, LSF9, and LSF8 samples, which can be deconvoluted into four peaks (Figure 4B), containing surface lattice oxygen (~528.5 eV, O_{lat}), adsorbed oxygen (~530.3 eV, ~531.4 eV, O_{ads}) and hydroxides and carbonates adsorbed in the molecular (~532.8 eV, OH^-/CO_3^{2-}).[20,48] The ratio of adsorbed oxygen in the total O species in LSF8 and LSF9 is less than LSF sample (Table S3), generated by the increase of the average valence states of Fe, which we think is another reason for the degradation of the electrochemical properties of composite materials. In addition, Figure 4C shows the Sr 3d spectrum of three samples, the lattice one indicates Sr in the perovskite oxide lattice, whereas the surface one includes Sr present on the surface state like $SrCO_3$. The ratio of $Sr_{lattice}/Sr_{surface}$ decreased from 6.79 in LSF to 3.00 in LSF8 (Table S4), The non-conductive $SrCO_3$ enriched on the surface will occupy the adsorption site of CO_2 and also affect the electrical conductivity of the samples as well as charge transportation process.

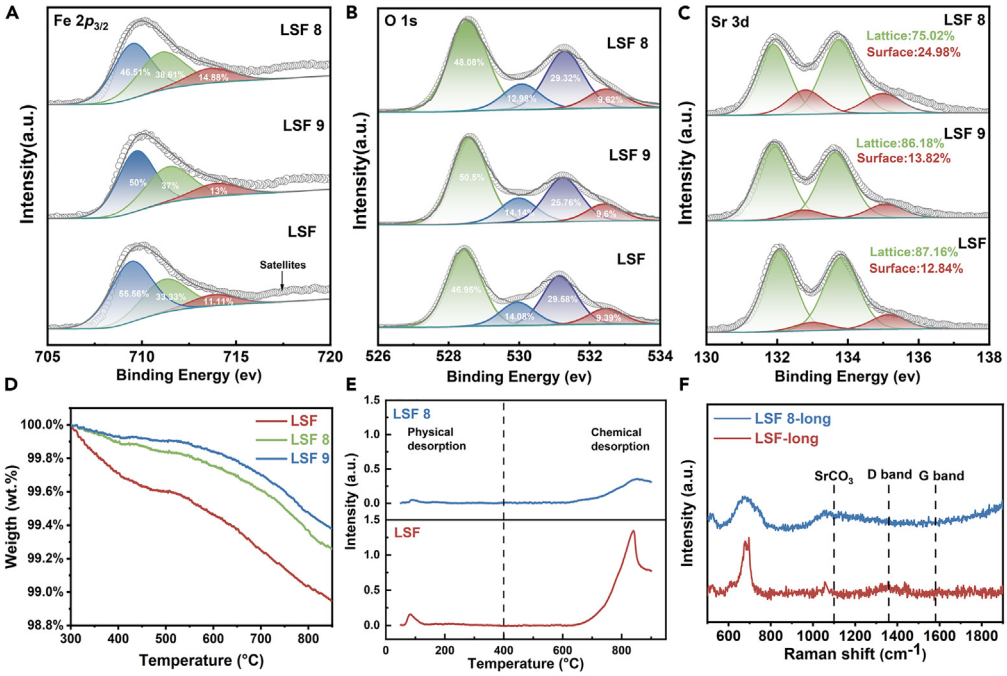

Figure 4. Physicochemical properties of LSF, LSF9, and LSF8 powders

(A–C) XPS of Fe $2p_{3/2}$, O 1s, and Sr 3d spectra.

(D) TG curves.

(E) CO_2-TPD curves.

(F) Raman of LSF and LSF8 surface after long-term stability test.

Therefore, the analysis of the Sr 3d spectrum can also explain the reason for the reduction of electrical conductivity and the possible reduced CO_2-RR electrochemical performance. The results of XPS indicate that the decrease in catalytic activity of the sample is the result of the increase of the average valence state of Fe, the decrease of surface oxygen vacancy, and the increase of surface $SrCO_3$ segregation.

Figure 4D shows the TG analysis results of three samples. The mass loss of LSF is far more than LSF9 and LSF8 at the temperature of 850°C. In other words, the intentional B-site defects lead to the reduction of oxygen vacancy content that is supposed to the active site for CO_2 chemical adsorption. Consequently, CO_2-TPD measurements were performed and the results are shown in Figure 4E. The peaks in the low temperature range can be summarized as a physical desorption signal, while peaks occurring in the high temperature range can be considered signals of chemical desorption.[21] All physical and chemical desorption signals of LSF8 are weaker than LSF. Specifically, chemical desorption decreases from 472 μmol g^{-1} for LSF to 170 μmol g^{-1} for LSF8 (Figure S10). This decrease in CO_2 adsorption capacity directly explains the reason for the large increase in low-frequency peak area in DRT figures which is related to gas adsorption and activation processes.

Although LSF-based materials have excellent catalytic activity in CO_2 reduction, they have always had stability problems in CO_2 electrolysis due to unstable phase transitions in redox atmospheres. Therefore, the XRD results of LSF and LSF8 powders after heat treatment in a 5:95 CO-CO_2 atmosphere for 2 h (respectively named LSF-C and LSF8-C, Figure S11) and the Raman test after long-term stability examination (Figure 4F) were also analyzed. According to XRD results, after treatment in a reducing atmosphere, $SrCO_3$ was observed in both LSF and LSF8 samples. Due to the excessive stoichiometric ratio of A-site elements in LSF8, the content of $SrCO_3$ segregated in LSF8 is even significantly higher than that in LSF, which can be judged according to the peak intensity of $SrCO_3$ (Figure S11). Interestingly, the RP phase originally present in LSF8 cannot detected by XRD after the treatment with a gas mixture. Sr elements in the rock salt layer in the RP phase have a greater dynamic tendency to segregate than that in the SP phase. In the latter phase, Sr is only located in the A-site of perovskite which also enabled the structural integrity of the SP phase under the reducing atmosphere, and consequently resulting in better stability of composite material in the process of CO_2 reduction. Nevertheless, there are no C-C bond signals (the band at 1588 and 1385 cm^{-1} can be due to the G-band and D-band of carbonaceous species) after a long time of operation on the LSF8 cathode.[48] Therefore, heterostructure materials show potential for practical applications in CO_2 utilization using SOEC technology.

Thus, in this work, we synthesized heterostructural single-phase (SP) perovskite/Ruddlesden–Popper (RP) phase perovskite from precursors of $La_{0.6}Sr_{0.4}Fe_{1-x}O_{3-\delta}$ (x = 0.1 and 0.2) perovskite oxides by intentionally adjusting B-site stoichiometry. Compared with $La_{0.6}Sr_{0.4}FeO_{3-\delta}$, SOECs based on the synthesized heterostructure electrode materials demonstrated a lower catalytic performance due to the low electrical conductivity of RP-LSF, the increase of the average valence state of Fe at B-site, more segregation of $SrCO_3$ as well as reduced oxygen vacancy and CO_2 adsorption capacity. This work provides a useful guide for the design of composite materials and offers a new perspective to study the electrochemical behavior of composite perovskite materials for CO_2-RR in SOEC. Future work will focus on investigating the effect of phase change under the typical *in situ* operational condition on the CO_2-RR electrochemical performance.

Limitations of the study

This study applies only to CO_2 electrolysis; the related method mentioned in the article might be used as a reference for other reactions in the future.

STAR★METHODS

Detailed methods are provided in the online version of this paper and include the following:

- KEY RESOURCES TABLE
- RESOURCE AVAILABILITY
  - Lead contact
  - Materials availability
  - Data and code availability
- EXPERIMENTAL MODEL AND SUBJECT DETAILS
- METHODS DETAILS
  - Material synthesis
  - Sample preparation
  - Materials characterization
  - Electrochemical test
- QUANTIFICATION AND STATISTICAL ANALYSIS
- ADDITIONAL RESOURCES

SUPPLEMENTAL INFORMATION

Supplemental information can be found online at https://doi.org/10.1016/j.isci.2024.109648.

ACKNOWLEDGMENTS

This work was financially supported by the National Natural Science Foundation of China (22378268), the Guangdong Basic and Applied Basic Research Foundation (2024A1515012212), and the National Taipei University of Technology-Shenzhen University (NTUT-SZU) Joint Research Program (2023011). The authors wish to acknowledge the assistance on TEM/STEM/FIB from the Instrumental Analysis Center of Shenzhen University (Xili Campus) and the Electron Microscopy Center of Shenzhen University.

AUTHOR CONTRIBUTIONS

Y.R. conducted the experiments and wrote the original paper. **L.W.** investigated, reviewed & edited the paper. **H.Y.** designed the experiments and reviewed & edited the paper. **S.M.** reviewed and edited the paper. **F.L.** provided the funding and resources and served as supervisor, reviewed, edited, and confirmed the final version of the paper.

DECLARATION OF INTERESTS

The authors declare no competing interests.

Received: February 8, 2024
Revised: March 5, 2024
Accepted: March 27, 2024
Published: March 29, 2024

REFERENCES

1. Hauch, A., Küngas, R., Blennow, P., Hansen, A.B., Hansen, J.B., Mathiesen, B.V., and Mogensen, M.B. (2020). Recent advances in solid oxide cell technology for electrolysis. Science *370*, eaba6118. https://doi.org/10.1126/science.aba6118.
2. Wu, A., Li, C., Han, B., Liu, W., Zhang, Y., Hanson, S., Guan, W., and Singhal, S.C. (2022). Pulsed electrolysis of carbon dioxide by large-scale solid oxide electrolytic cells for intermittent renewable energy storage. Carbon Energy *5*, e262. https://doi.org/10.1002/cey2.262.
3. Zheng, Y., Wang, J., Yu, B., Zhang, W., Chen, J., Qiao, J., and Zhang, J. (2017). A review of high temperature co-electrolysis of H_2O and CO_2 to produce sustainable fuels using solid oxide electrolysis cells (SOECs): advanced materials and technology. Chem. Soc. Rev. *46*, 1427–1463. https://doi.org/10.1039/C6CS00403B.
4. Song, Y., Zhang, X., Xie, K., Wang, G., and Bao, X. (2019). High-temperature CO_2 electrolysis in solid oxide electrolysis cells: Developments, challenges, and prospects. Adv. Mater. *31*, e1902033. https://doi.org/10.1002/adma.201902033.
5. Lee, S., Kim, M., Lee, K.T., Irvine, J.T.S., and Shin, T.H. (2021). Enhancing electrochemical CO_2 reduction using Ce(Mn,Fe)O_2 with La(Sr)Cr(Mn)O_3 cathode for high-temperature solid oxide electrolysis cells. Adv. Energy Mater. *11*, 2100339. https://doi.org/10.1002/aenm.202100339.
6. Zhou, X., Yang, J., Wang, R., Zhang, W., Yun, S., and Wang, B. (2022). Advances in lithium-ion battery materials for ceramic fuel cells. Energy Mater *2*, 200041. https://doi.org/10.20517/energymater.2022.76.
7. Xie, M., Cai, C., Duan, X., Xue, K., Yang, H., and An, S. (2024). Review on Fe-based double perovskite cathode materials for solid oxide fuel cells. Energy Mater. *4*, 400007. https://doi.org/10.20517/energymater.2023.70.

8. Jiang, Y., Chen, F., and Xia, C. (2021). A review on cathode processes and materials for electro-reduction of carbon dioxide in solid oxide electrolysis cells. J. Power Sources *493*, 229713. https://doi.org/10.1016/j.jpowsour.2021.229713.
9. Wang, N., Huang, Z.Y., Tang, C.M., Xing, L.X., Meng, L., Aoki, Y., Du, L., and Ye, S.Y. (2023). Functional layer engineering to improve performance of protonic ceramic fuel cells. Rare Met. *42*, 2250–2260. https://doi.org/10.1007/s12598-022-02257-x.
10. Hu, S., Zhang, L., Liu, H., Li, W., Cao, Z., Cai, L., Zhu, Y., Zhu, X., and Yang, W. (2019). Detrimental phase evolution triggered by Ni in perovskite-type cathodes for CO_2 electroreduction. J. Energy Chem. *36*, 87–94. https://doi.org/10.1016/j.jechem.2019.06.001.
11. Tan, T., Wang, Z., Qin, M., Zhong, W., Hu, J., Yang, C., and Liu, M. (2022). In Situ Exsolution of Core-Shell Structured NiFe/FeO_x Nanoparticles on $Pr_{0.4}Sr_{1.6}(NiFe)_{1.5}Mo_{0.5}O_{6-\delta}$ for CO_2 Electrolysis. Adv. Funct. Mater. *32*, 2202878. https://doi.org/10.1002/adfm.202202878.
12. Monika, S., Sara, P., Akhilesh Kumar, S., Ranjan, S., Aradhana, S., and Manish, S. (2024). Recent advancement of solid oxide fuel cells towards semiconductor membrane fuel cells. Energy Mater *4*, 400012. https://doi.org/10.20517/energymater.2023.54.
13. Sunarso, J., Hashim, S.S., Zhu, N., and Zhou, W. (2017). Perovskite oxides applications in high temperature oxygen separation, solid oxide fuel cell and membrane reactor: A review. Prog. Energy Combust. Sci. *61*, 57–77. https://doi.org/10.1016/j.pecs.2017.03.003.
14. Luo, Y., Liu, T., Wang, Y., and Ding, M. (2023). High-temperature CO_2 electrolysis in solid oxide electrolysis cells cathode: Advances and perspective. Chem Catal. *3*, 100815. https://doi.org/10.1016/j.checat.2023.100815.
15. Ye, L., Zhang, M., Huang, P., Guo, G., Hong, M., Li, C., Irvine, J.T.S., and Xie, K. (2017). Enhancing CO_2 electrolysis through synergistic control of non-stoichiometry and doping to tune cathode surface structures. Nat. Commun. *8*, 14785. https://doi.org/10.1038/ncomms14785.
16. Li, Y., Chen, X., Yang, Y., Jiang, Y., and Xia, C. (2017). Mixed-Conductor $Sr_2Fe_{1.5}Mo_{0.5}O_{6-\delta}$ as Robust Fuel Electrode for Pure CO_2 Reduction in Solid Oxide Electrolysis Cell. ACS Sustain. Chem. Eng. *5*, 11403–11412. https://doi.org/10.1021/acssuschemeng.7b02511.
17. Xi, X., Liu, J., Luo, W., Fan, Y., Zhang, J., Luo, J., and Fu, X. (2021). Unraveling the Enhanced Kinetics of $Sr_2Fe_{1+x}Mo_{1-x}O_{6-\delta}$ Electrocatalysts for High-Performance Solid Oxide Cells. Adv. Energy Mater. *11*, 2102845. https://doi.org/10.1002/aenm.202102845.
18. Hu, F., Chen, K., Ling, Y., Huang, Y., Zhao, S., Wang, S., Gui, L., He, B., and Zhao, L. (2024). Smart Dual-Exsolved Self-Assembled Anode Enables Efficient and Robust Methane-Fueled Solid Oxide Fuel Cells. Adv. Sci. *11*, 2306845. https://doi.org/10.1002/advs.202306845.
19. Zhang, X., Song, Y., Guan, F., Zhou, Y., Lv, H., Liu, Q., Wang, G., and Bao, X. (2018). $(La_{0.75}Sr_{0.25})_{0.95}(Cr_{0.5}Mn_{0.5})O_{3-\delta}$-$Ce_{0.8}Gd_{0.2}O_{1.9}$ scaffolded composite cathode for high temperature CO_2 electroreduction in solid oxide electrolysis cell. J. Power Sources *400*, 104–113. https://doi.org/10.1016/j.jpowsour.2018.08.017.
20. Lin, W., Su, W., Li, Y., Chiu, T.W., Singh, M., Pan, Z., and Fan, L. (2023). Enhancing Electrochemical CO_2 Reduction on Perovskite Oxide for Solid Oxide Electrolysis Cells through In Situ A-Site Deficiencies and Surface Carbonate Deposition Induced by Lithium Cation Doping and Exsolution. Small *19*, 2303305. https://doi.org/10.1002/smll.202303305.
21. Zhang, S., Yang, C., Jiang, Y., Li, P., and Xia, C. (2023). A robust fluorine-containing ceramic cathode for direct CO_2 electrolysis in solid oxide electrolysis cells. J. Energy Chem. *77*, 300–309. https://doi.org/10.1016/j.jechem.2022.10.021.
22. Zhang, P., Chang, J., Qu, F., Tang, Y., Jing, J., Wang, H., Chen, L., Xing, S., and Yang, Z. (2024). Clean and Sustainable Power to X to Power by Reversible Symmetrical Solid Oxide Cells with Highly Active Ferrite Perovskite Electrodes. ACS Sustain. Chem. Eng. *12*, 1561–1572. https://doi.org/10.1021/acssuschemeng.3c06791.
23. Lin, W., Li, Y., Singh, M., Zhao, H., Yang, R., Su, P.-C., and Fan, L. (2024). Electronic engineering and oxygen vacancy modification of $La_{0.6}Sr_{0.4}FeO_{3-\delta}$ perovskite oxide by low-electronegativity sodium substitution for efficient CO_2/CO fueled reversible solid oxide cells. Green Chem. *26*, 3202–3210. https://doi.org/10.1039/D3GC04451C.
24. He, F., Hou, M., Zhu, F., Liu, D., Zhang, H., Yu, F., Zhou, Y., Ding, Y., Liu, M., and Chen, Y. (2022). Building Efficient and Durable Hetero-Interfaces on a Perovskite-Based Electrode for Electrochemical CO_2 Reduction. Adv. Energy Mater. *12*, 2202175. https://doi.org/10.1002/aenm.202202175.
25. Wang, S., Qian, B., Tang, Y., Ni, Q., Zheng, Y., Chen, H., Ge, L., and Yang, H. (2023). Enhanced oxygen bulk diffusion of $La_{0.6}Sr_{0.4}FeO_{3-\delta}$ fuel electrode by high valence transition metal doping for direct CO_2 electrolysis in solid oxide electrolysis cells. Electrochim. Acta *439*, 141659. https://doi.org/10.1016/j.electacta.2022.141659.
26. Li, Y., Li, Y., Wan, Y., Xie, Y., Zhu, J., Pan, H., Zheng, X., and Xia, C. (2019). Perovskite oxyfluoride electrode enabling direct electrolyzing carbon dioxide with excellent electrochemical performances. Adv. Energy Mater. *9*, 1803156. https://doi.org/10.1002/aenm.201803156.
27. Ding, X., Gao, Z., Ding, D., Zhao, X., Hou, H., Zhang, S., and Yuan, G. (2019). Cation deficiency enabled fast oxygen reduction reaction for a novel SOFC cathode with promoted CO_2 tolerance. Appl. Catal., B *243*, 546–555. https://doi.org/10.1016/j.apcatb.2018.10.075.
28. Zhao, G., Rui, K., Dou, S.X., and Sun, W. (2018). Heterostructures for Electrochemical Hydrogen Evolution Reaction: A Review. Adv. Funct. Mater. *28*, 1803291. https://doi.org/10.1002/adfm.201803291.
29. Qiu, P., Li, C., Liu, B., Yan, D., Li, J., and Jia, L. (2023). Materials of solid oxide electrolysis cells for H_2O and CO_2 electrolysis: A review. J. Adv. Ceram. *12*, 1463–1510. https://doi.org/10.26599/Jac.2023.9220767.
30. Li, Y., Li, Y., Zhang, S., Ren, C., Jing, Y., Cheng, F., Wu, Q., Lund, P., and Fan, L. (2022). Mutual conversion of CO-CO_2 on a perovskite fuel electrode with endogenous alloy nanoparticles for reversible solid oxide cells. ACS Appl. Mater. Interfaces *14*, 9138–9150. https://doi.org/10.1021/acsami.1c23548.
31. Li, Y., Singh, M., Zhuang, Z., Jing, Y., Li, F., Maliutina, K., He, C., and Fan, L. (2021). Efficient reversible CO/CO_2 conversion in solid oxide cells with a phase-transformed fuel electrode. Sci. China Mater. *64*, 1114–1126. https://doi.org/10.1007/s40843-020-1531-7.
32. Xi, X., Fan, Y., Zhang, J., Luo, J.-L., and Fu, X.-Z. (2022). In situ construction of hetero-structured perovskite composites with exsolved Fe and Cu metallic nanoparticles as efficient CO_2 reduction electrocatalysts for high performance solid oxide electrolysis cells. J. Mater. Chem. A *10*, 2509–2518. https://doi.org/10.1039/D1TA07678G.
33. Li, Y., Yu, L., Yu, Y., Maliutina, K., Wu, Q., He, C., and Fan, L. (2021). Understanding CO_2 electrochemical reduction kinetics of mixed-conducting cathodes by the electrical conductivity relaxation method. Int. J. Hydrogen Energy *46*, 9646–9652. https://doi.org/10.1016/j.ijhydene.2020.07.141.
34. Demont, A., Sayers, R., Tsiamtsouri, M.A., Romani, S., Chater, P.A., Niu, H., Martí-Gastaldo, C., Xu, Z., Deng, Z., Bréard, Y., et al. (2013). Single Sublattice Endotaxial Phase Separation Driven by Charge Frustration in a Complex Oxide. J. Am. Chem. Soc. *135*, 10114–10123. https://doi.org/10.1021/ja403611s.
35. Song, Y., Chen, Y., Xu, M., Wang, W., Zhang, Y., Yang, G., Ran, R., Zhou, W., and Shao, Z. (2020). A Cobalt-Free Multi-Phase Nanocomposite as Near-Ideal Cathode of Intermediate-Temperature Solid Oxide Fuel Cells Developed by Smart Self-Assembly. Adv. Mater. *32*, e1906979. https://doi.org/10.1002/adma.201906979.
36. Hu, F., Ling, Y., Fang, S., Sui, L., Xiao, H., Huang, Y., Wang, S., He, B., and Zhao, L. (2023). Engineering dual-exsolution on self-assembled cathode to achieve efficient electrocatalytic CO_2 reduction. Appl. Catal., B *337*, 122968. https://doi.org/10.1016/j.apcatb.2023.122968.
37. Li, Y., Li, Y., Yu, L., Hu, Q., Wang, Q., Maliutina, K., and Fan, L. (2021). Achieving excellent and durable CO_2 electrolysis performance on a dual-phase fuel electrode in solid oxide electrolysis cells. J. Power Sources *491*, 229599. https://doi.org/10.1016/j.jpowsour.2021.229599.
38. Zhang, B.W., Zhu, M.N., Gao, M.R., Xi, X., Duan, N., Chen, Z., Feng, R.F., Zeng, H., and Luo, J.L. (2022). Boosting the stability of perovskites with exsolved nanoparticles by B-site supplement mechanism. Nat. Commun. *13*, 4618. https://doi.org/10.1038/s41467-022-32393-y.
39. Hong, K., Choi, M., Bae, Y., Min, J., Lee, J., Kim, D., Bang, S., Lee, H.-K., Lee, W., and Hong, J. (2023). Direct methane protonic ceramic fuel cells with self-assembled Ni-Rh bimetallic catalyst. Nat. Commun. *14*, 7485. https://doi.org/10.1038/s41467-023-43388-8.
40. Meng, Y., Akbar, M., Gao, J., Singh, M., Chiu, T.-W., Wang, B., Xia, C., and Fan, L. (2024). Superionic conduction of self-assembled heterostructural LSCrF-CeO_2 electrolyte for solid oxide fuel cell at 375–550 °C. Appl. Surf. Sci. *645*, 158832. https://doi.org/10.1016/j.apsusc.2023.158832.
41. Ungár, T. (2004). Microstructural parameters from X-ray diffraction peak broadening. Scripta Mater. *51*, 777–781. https://doi.org/10.1016/j.scriptamat.2004.05.007.
42. Lou, H., Zhang, H., Yao, C., Chen, M., Xia, B., Zhang, Z., Sun, Y., Lang, X., and Cai, K. (2024).

Nd-doping-induced perovskite/Ruddlesden-Popper heterointerfaces boost the ORR activity and CO_2 tolerance for $SrFeO_3$–based cathode. Ceram. Int. *50*, 2249–2258. https://doi.org/10.1016/j.ceramint.2023.10.343.

43. Xiong, D., Rasaki, S.A., Li, Y., Fan, L., Liu, C., and Chen, Z. (2022). Enhanced cathodic activity by tantalum inclusion at B-site of $La_{0.6}Sr_{0.4}CO_{0.4}Fe_{0.6}O_3$ based on structural property tailored via camphor-assisted solid-state reaction. J. Adv. Ceram. *11*, 1330–1342. https://doi.org/10.1007/s40145-022-0627-x.
44. Zhou, R., Yin, Y., Dai, H., Yang, X., Gu, Y., and Bi, L. (2023). Attempted preparation of $La_{0.5}Ba_{0.5}MnO_{3-\delta}$ leading to an in-situ formation of manganate nanocomposites as a cathode for proton-conducting solid oxide fuel cells. J. Adv. Ceram. *12*, 1189–1200. https://doi.org/10.26599/jac.2023.9220748.
45. Dong, K., Hou, J., Miao, L., Jin, Z., Wang, D., Teng, Y., and Liu, W. (2020). A comparative study of the R-P phase $Sr_{n+1}Fe_nO_{3n+1}$ (n= 1, 2 and 3) cathodes for intermediate temperature solid oxide fuel cells. Ceram. Int. *46*, 19335–19342. https://doi.org/10.1016/j.ceramint.2020.04.274.
46. Liu, C., Li, S., Gao, J., Bian, L., Hou, Y., Wang, L., Peng, J., Bao, J., Song, X., and An, S. (2021). Enhancing CO_2 Catalytic Adsorption on an Fe Nanoparticle-Decorated $LaSrFeO_{4+\delta}$ Cathode for CO_2 Electrolysis. ACS Appl. Mater. Interfaces *13*, 8229–8238. https://doi.org/10.1021/acsami.0c18997.
47. Zhang, X., Liu, L., Zhao, Z., Tu, B., Ou, D., Cui, D., Wei, X., Chen, X., and Cheng, M. (2015). Enhanced oxygen reduction activity and solid oxide fuel cell performance with a nanoparticles-loaded cathode. Nano Lett. *15*, 1703–1709. https://doi.org/10.1021/nl5043566.
48. Deka, D.J., Kim, J., Gunduz, S., Jain, D., Shi, Y., Miller, J.T., Co, A.C., and Ozkan, U.S. (2021). Coke formation during high-temperature CO_2 electrolysis over $AFeO_3$ (A = La/Sr) cathode: Effect of A-site metal segregation. Appl. Catal., B *283*, 119642. https://doi.org/10.1016/j.apcatb.2020.119642.

STAR★METHODS

KEY RESOURCES TABLE

REAGENT or RESOURCE	SOURCE	IDENTIFIER
Chemicals, peptides, and recombinant proteins		
Lanthanum nitrate hexahydrate	Shanghai Macklin Biochemical Technology Co., Ltd	E1722137; CAS:10277-43-7
Strontium nitrate	Aladdin Industrial Corporation	I1712036; CAS:10042-76-9
Ferric nitrate	Shanghai Macklin Biochemical Technology Co., Ltd	C15518746; CAS:7782-61-8
LSGM-8282	Wuxi City Kaistar Electro-Optic Materials Co., Ltd.	N/A

RESOURCE AVAILABILITY

Lead contact

Further information and requests for resources should be directed to and will be fulfilled by the lead contact, Liangdong Fan (fanld@szu.edu.cn).

Materials availability

The study did not generate new unique materials. The readers can buy the chemicals to remake the materials as mentioned in the text.

Data and code availability

- Data: All data reported in this paper will be shared by the lead contact upon request.
- Code: This paper does not report the original code.
- Any additional information required to reanalyze the data reported in this paper is available from the lead contact upon request.

EXPERIMENTAL MODEL AND SUBJECT DETAILS

There are no experimental models (animals, human subjects, plants, microbe strains, cell lines, primary cell cultures) used in the study.

METHODS DETAILS

Material synthesis

$La_{0.6}Sr_{0.4}FeO_{3-\delta}$ (LSF), $La_{0.6}Sr_{0.4}Fe_{0.9}O_{3-\delta}$ (LSF9), and $La_{0.6}Sr_{0.4}Fe_{0.8}O_{3-\delta}$ (LSF8) powders were prepared by the classic sol-gel method as below. The starting materials, $La(NO_3)_2{\cdot}6H_2O$ (99%, Macklin), $Sr(NO_3)_2$ (≥99.0%, Aladdin), and $Fe(NO_3)_2$ (98.5%, Macklin), were dissolved in the beaker by deionized water with stoichiometric ratios. Then, citric acid monohydrate (CA, 99.5%, Aladdin) and ethylene diamine tetra-acetic acid (EDTA, 99.5%, Aladdin) were added as the complexing and combustion agents. The molar ratio of total metal ions, CA, and EDTA was set to 1:2:1. Eventually, ammonia was added to adjust the pH of the solution to 7-8 for absolutely dissolved salt nitrate. After 24 h of stirring, the precursor solution was transferred to evaporating dish and dried at 200 °C, until the organic matter burned out and the precursor powder was obtained. The precursor powder was calcined in air at 1000 °C for 5 h to gain the black powder with a perovskite structure.

The preparation method of anode powder, $La_{0.6}Sr_{0.4}Co_{0.2}Fe_{0.8}O_{3-\delta}$, is the same as above but using the starting materials $La(NO_3)_2{\cdot}6H_2O$ (99%, Macklin), $Sr(NO_3)_2$ (≥99.0%, Aladdin), $Fe(NO_3)_2$ (98.5%, Macklin), $Co(NO_3)_2{\cdot}6H_2O$ (99%, Aladdin), CA (99.5%, Aladdin) and EDTA (99.5%, Aladdin), abd the calcination temperature and duration change to 900°C for 5 h. To improve the conductivity of oxygen ions, $Sm_{0.2}Ce_{0.8}O_{2-\delta}$ (SDC), a high oxygen ion conductor, was added. SDC was synthesized by glycine combustion method with the precursor calcined at 600°C for 2 h. The LSCF-SDC (50:50 wt. %) composite sample was obtained by ball milling for 24 h.

Sample preparation

The electrolyte-supported single cells with LSFx | LSGM | LSCF-SDC were used to demonstrate electrochemical performance. The LSGM electrolytes were formed by dry-pressing LSGM powder (Wuxi City Kaistar Electro-Optic Materials Co., Ltd.) which is mixed with 3 wt.% PVA (polyvinyl alcohol) by grinding for 2 h and then calcined at 1450 °C for 6 h to obtain the dense electrolyte (~ 220 μm). The air electrode slurry was obtained by mixing LSCF-SDC powders and terpineol (containing 6 wt.% methyl-cellulose) for 1 h. The fuel electrode slurries, LSF / LSF9 / LSF8, were obtained in the same way. The slurries were printed onto LSGM electrolytes by screen print method and then co-fired at 1000 °C for 2 h in air. The symmetric cells were prepared in the same way while both sides were LSFx fuel electrodes. After sintering, silver paste (Guiyan Platinum Industry Co., LTD) was printed onto electrodes (0.2826 cm^2) as the current collector.

LSF and LSF8 bar samples were prepared for the electrical conductivity test. 1 g LSF or LSF8 powders mixed with 3 wt.% PVA was ground in a mortar for 1 h, then the bars formed by the dry-press process. In the end, the bars were calcined at 1300°C in air for 6 h to achieve the required density for electrical conductivity testing.

Materials characterization

The phase structure of all materials was characterized by XRD (PANalytical, Empyrean) with Cu Kα radiation and TEM (JEOL, JEM-2100 & X-Max80). The crystal structure parameters and phase proportion of LSFx were fitted by GSAS refinement. The micromorphology of powders was observed by SEM (HIT, S-3400N). The electrical conductivity was measured in air and 95: 5 CO_2-CO by a four-paragraph method using a conductivity meter (KEITHLEY). The surface properties of powder samples were characterized by X-ray photoelectron spectroscopy (XPS, Thermo Fisher Scientific, K-Alpha+). The high-temperature physical and chemical properties of powder samples were detected by Thermo Gravimetric Analysis (TGA, Mettler, TGA\DSC 3+). Raman spectrometer (Renishaw) was used to determine the coke formation on the fuel electrode powders' surface after long-term examination. CO_2-TPD was used to study the CO_2 adsorption capacity of LSF and LSF8 samples.

Electrochemical test

The single SOEC was sealed at the top of the Al_2O_3 tube using Cerama-bond 552-VFG sealant (Aremco). The fuel electrode was exposed to pure CO_2 while the air electrode was exposed directly to the atmosphere for the SOEC test. The flow rate of pure CO_2 was 50 ml min^{-1}. An electrochemical workstation (VersaSTAT 4) was used to evaluate the electrochemical performance; the applied voltage window is from open-circuit voltage to 1.6 V at a scan rate of 10 mV s^{-1} for CO_2 electrolysis. The short-term CO_2 electrolysis stability test was operated at 1.2, 1.3, 1.4, and 1.5 V, each was stabilized for 20 min at 800°C. The long-term CO_2 electrolysis stability test was operated at a constant voltage of 1.1 V at 800°C. EIS measurement of a single SOEC was obtained in the frequency range of 10^5 Hz to 0.1 Hz with an AC amplitude of 20 mV. The symmetric cell's EIS measurement was obtained in the frequency range of 10^5 Hz to 0.1 Hz with an AC amplitude of 10 mV, but it is under a 1: 1 CO–CO_2 atmosphere. EIS data of single SOEC and symmetric cells were collected at 750-850°C.

The gas product was determined by the online gas chromatography (GC-2014, SHIMADZU) equipped with a thermal conductivity cell detector (TCD). The gas flow rate was determined by a flowmeter. The faradaic efficiency was calculated by the following Equation.[19,20,31,32]

$$FE_{CO} = \frac{n_{CO,measured}}{I \times (n \times F)^{-1}} \times 100\%$$

Where $n_{CO,\ measured}$ (mol s^{-1}) is the measured carbon monoxide production rate in the exhaust gas from the electrochemical cell (GC data). I (A) is the current, n is 2 and F is Faraday's constant (96485 C mol^{-1}).

QUANTIFICATION AND STATISTICAL ANALYSIS

No methods were used to determine whether the data met the assumptions of the statistical approach.

ADDITIONAL RESOURCES

Our study has not generated or contributed to a new website/forum or has not been part of a clinical trial.